

# A HIGH-RESOLUTION SCALABLE MESHLESS METHOD FOR COUPLED STEADY POROELASTIC ANALYSIS, BASED ON COLLOCATION WITH RADIAL BASIS FUNCTIONS

HENRY POWER<sup>\*</sup>, DAVID STEVENS<sup>\*</sup> AND K. ANDREW CLIFFE<sup>†</sup>

<sup>\*</sup> Faculty of Engineering, Department of Mechanical, Materials and Manufacturing Engineering  
University of Nottingham, University Park, Nottingham, UK  
e-mail: henry.power@nottingham.ac.uk

<sup>†</sup> School of Mathematical Sciences  
University of Nottingham, University Park, Nottingham, UK

**Key words:** Radial Basis Functions, Meshless, Poroelasticity, Finite Collocation

**Abstract.** This work describes the application of a novel meshless numerical technique, based on local collocation with radial basis functions (RBFs), to the solution of steady poroelastic problems. Its formulation allows scalability to large problem sizes, in contrast to traditional full-domain RBF collocation methods which are restricted to small datasets due to issues with numerical conditioning and computational cost. The proposed method is validated using a benchmark linear elasticity numerical example and a coupled steady poroelastic deformation problem, for which analytical solutions are known. Highly accurate solutions are obtained in each case, and convergence rates in excess of sixth-order are observed.

## 1 INTRODUCTION

The interaction between fluid flow and porous matrix deformation is known as hydromechanical coupling, where the porous matrix can deform as a result of either changes in external loads, or internal pore pressures. Poroelasticity describes the governing equation for porous matrix deformation in terms of a non-homogeneous Navier system of equations for linear elasticity, with the non-homogeneous term given by the gradient of the fluid pressure. Similarly, the stress tensor constitutive equation is given by the linear elastic stress tensor minus the fluid pressure. The fluid mass balance equation occupying the void space must also account for the motion due to the solid deformation, resulting in a set of coupled partial differential equations. By neglecting the compressibility of the pore fluid and soil matrix, and considering steady state conditions, the doubly-coupled problem reduces to a one way coupling with a forcing term proportional to the pressure gradient in the solid deformation governing equation.

In this work we implement a novel local RBF collocation method (RBF-FC approach), recently developed in [1], to solve the coupled problem of flow and solid matrix deformation in poroelasticity. The basic RBF collocation method for the solution of PDEs was originally described by Kansa [2, 3], and has been successfully applied to a wide range of PDEs. RBF collocation methods are attractive due to their meshless formulation, ease of implementation, high convergence rates, and flexibility to enforce arbitrary boundary conditions. However the use of globally supported basis functions leads to fully-populated collocation matrices, which

become increasingly ill-conditioned and computationally expensive with increasing dataset size. These limitations motivate the development of alternate methods to mitigate the computational cost and numerical conditioning issues, while maintaining the performance and flexibility of the full-domain formulation.

One of the most efficient ways to overcome the ill-conditioning problem is the use of a generalised finite difference method based on RBF collocation (RBF-FD method), where a small interpolation stencil is constructed around each data point within the domain, which connects the point to its neighbours. In this way a large number of highly overlapping local collocation systems are formed. In analogy to traditional finite difference methods, the local RBF systems collocate the unknown solution value at each internal node included within the system, with the governing PDE enforced by reconstruction to form a sparse global linear system that expresses the governing PDE operator in terms of surrounding nodal values. Unlike traditional polynomial-based FD methods, RBF-FD methods can operate effectively on irregular datasets. For more information on RBF-FD methods see, for example, [4, 5, 6, 7].

In [1] an alternative RBF localisation is proposed for the meshless solution of PDEs, which is referred to as the RBF finite collocation approach (RBF-FC). As with the RBF-FD approach, small overlapping collocation stencils are formed around each internal node. However, the proposed method does not use the finite difference principle to drive the solution of the PDE; the PDE and boundary operators are enforced only within the local collocation systems, and are not used to generate the sparse global system. The global system is instead obtained by reconstructing the (Dirichlet) value of the field-variable, thereby describing the solution at the system centrepoin in terms of the unknown solution values at surrounding nodes. In this way the enforcement of the governing PDE and boundary operators is handled entirely within the local systems; the solution is driven by collocation and not by finite difference reconstruction.

## 2 LINEAR POROELASTICITY

The theory of poroelasticity was essentially developed by Maurice A. Biot. In [8], he couples Navier's linear elasticity equations with Darcy's law for the flow through a porous medium. In the present work, steady state solutions of the Biot equations are considered for an isotropic material and incompressible fluid. Under these conditions, the equations modelling the displacement  $u_i$  of the material and the pressure  $p$  of the fluid can be written:

$$\frac{\partial}{\partial x_i} \left( \frac{k(x)}{\mu} \frac{\partial (p - \rho g x_2)}{\partial x_j} \right) = 0 \quad (1)$$

where the pressure distribution,  $p$ , is defined by the steady Darcy flow, with an isotropic permeability  $k(x)$ , fluid viscosity  $\mu$ , gravity acceleration  $g$  and where  $x_2$  is the vertical coordinate, taken positive upwards.

The poroelastic stress-tensor is given by

$$\sigma_{ij} = \lambda \varepsilon_{kk} \delta_{ij} + 2\mu \varepsilon_{ij} - \alpha p \delta_{ij} \quad (2)$$

where  $\alpha \in [0, 1]$  is the Biot coefficient,  $\varepsilon_{ij}$  is the infinitesimal strain tensor

$$\varepsilon_{ij} = \frac{1}{2} \left( \frac{\partial u_i}{\partial x_j} + \frac{\partial u_j}{\partial x_i} \right) \quad (3)$$

and  $\lambda$ ,  $\mu$ , are the Lamé constants which, for plane-strain, are related to the Young's modulus ( $E$ ) and Poisson ratio ( $\nu$ ) as:

$$\lambda = \frac{E\nu}{(1+\nu)(1-2\nu)}, \quad \mu = \frac{E}{2(1+\nu)}. \quad (4)$$

The stress field satisfies the momentum equation

$$\frac{\partial \sigma_{ij}}{\partial x_j} = 0 \quad (5)$$

Writing the stress tensor in terms of the effective stress as

$$\sigma_{ij} = \tilde{\sigma}_{ij} - \alpha p \delta_{ij} \quad (6)$$

and substituting into equation (5), the following non-homogeneous equation is found:

$$\frac{\partial \tilde{\sigma}_{ij}}{\partial x_j} = \alpha \frac{\partial p}{\partial x_i}. \quad (7)$$

In the above equation, the pressure field and its gradient are computed from the solution of the Darcy flow equation (1), and are coupled with the elasticity equation.

### 3 A NOVEL MESHLESS LOCAL COLLOCATION STRATEGY FOR HIGH CONVERGENCE SOLUTIONS OF PORO-ELASTICITY PROBLEMS

To facilitate the locally-driven solution of the PDE, the RBF-FC local collocation systems are somewhat different from those used in RBF-FD methods. Rather than collocating the solution value at all nodes within the local stencil, the solution value is collocated only over the periphery of the stencil.

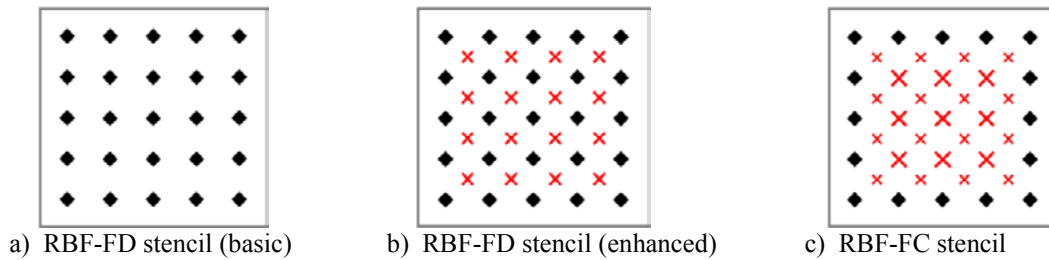


Figure 1: Comparison of collocation stencils for RBF finite difference, and the finite collocation approach.

- Black marks represent collocation of the unknown solution value (solution centres)
- Red crosses represent collocation of the PDE governing operator (PDE centres)

In this way the local stencils communicate only via their boundaries, and the resulting finite collocation method is more strongly related to traditional RBF domain decomposition

overlapping approaches; e.g. [9]. Within the interior of the stencils the PDE governing operator is collocated. In the case that the stencil lies sufficiently close to a domain boundary, collocation of the boundary operator replaces collocation of the solution field along the appropriate stencil boundary. The difference between the stencils used in RBF-FD methods and those of the proposed finite collocation method is outlined in Figure 1.

### 3.1 Kansa Collocation for linear scalar problems

A radial basis function depends upon the separation distances of a set of functional centres, exhibiting spherical symmetry around these centres. There are several commonly used radial basis functions (see [10]), however we will use the multiquadric RBF throughout, with  $m=1$ .

$$\psi(r) = (r^2 + c^2)^{\frac{m}{2}} \quad m \in \mathfrak{T}^+ \quad (8)$$

The  $c$  term is known as the ‘shape parameter’, and describes the relative width of the RBF functions about their centres. In practice, tuning of this parameter can dramatically affect the quality of the solution obtained, and much research has been directed towards finding effective methods of optimisation (see for example [11,12]). Since  $c$  is a length scale it is appropriate to consider a non-dimensional alternative,  $c^* = c/\Delta$ , where  $\Delta$  is typically related to the node separation distance in some way.

The Kansa RBF collocation method [2, 3], constructs the continuous solution  $u(x)$  of the PDE from a distinct set of  $N$  quasi-randomly distributed functional centres  $\xi_d$ :

$$u(x) = \sum_{j=1}^N \alpha_j \psi(\|x - \xi_j\|) + \sum_{j=1}^{NP} \alpha_{j+N} P_{m-1}^j(x) \quad x \in \mathfrak{R}^n \quad (9)$$

Here  $P_{m-1}^j$  is the  $j^{\text{th}}$  term of an order  $(m-1)$  polynomial, under the constraint

$$\sum_{j=1}^N \alpha_j P_{m-1}^k(x_j) = 0 \quad k = 1, \dots, NP \quad (10)$$

Consider a typical linear boundary value problem

$$\begin{aligned} L[u] &= f(x) && \text{on } \Omega \\ B[u] &= g(x) && \text{on } \partial\Omega \end{aligned} \quad (11)$$

where the operators  $L[\ ]$  and  $B[\ ]$  are linear partial differential operators on the domain  $\Omega$  and on the boundary  $\Gamma$ , describing the governing equation and boundary conditions respectively. Collocating the interpolation formula (9) at  $N$  distinct locations,  $x_j$ , coinciding with the functional centres  $\xi_d$ , leads to a system of equations

$$\begin{bmatrix} B[\psi] & B[P_{m-1}] \\ L[\psi] & L[P_{m-1}] \\ P_{m-1} & 0 \end{bmatrix} \alpha = \begin{bmatrix} g \\ f \\ 0 \end{bmatrix} \quad (12)$$

which is fully populated and non-symmetric. This approach, known as Kansa’s method, has been applied to a wide range of problems with great success (see for example [13, 14, 15]).

### 3.2 Kansa collocation for non-homogeneous linear elasticity

For coupled multivariate PDEs the basic RBF collocation formulae (9), (10) must be modified slightly. The following demonstrates the application to linear elasticity, however the same principles may be used to construct a global collocation for any linear multivariate PDE.

The non-homogeneous Lamé-Navier equations for linear elastic deformation, equation (7), in terms of displacement,  $u_i$ , are given by

$$(\lambda + \mu) \frac{\partial^2 u_j}{\partial x_i \partial x_j} + \mu \frac{\partial^2 u_i}{\partial x_j^2} = -\rho b_i \quad (13)$$

for a given body force  $b_i$  (in the case of poroelasticity  $\rho b_i = \alpha \partial p / \partial x_i$ ) and material density  $\rho$ . Here  $\lambda$  and  $\mu$  are the Lamé coefficients as defined in (4). For a 2D plane-stress approximation, the value of  $\lambda$  should instead be changed to:

$$\lambda^* = \frac{E\nu}{(1-\nu^2)} \quad (14)$$

Boundary conditions are applied either as a fixed displacement (Dirichlet condition), i.e.,

$$u_i = f_i \quad (15)$$

or as a prescribed surface traction (Neumann condition). The surface-traction operator at a surface with unit outward normal  $n_i$  and an applied traction  $\tau_i$ , is given by:

$$\lambda n_i \frac{\partial u_k}{\partial x_k} + \mu n_j \left( \frac{\partial u_i}{\partial x_j} + \frac{\partial u_j}{\partial x_i} \right) = \tau_i \quad (16)$$

The solution construction is similar to that of the single-variable formulation:

$$u_i(x) = \sum_{j=1}^N \alpha_{i,j} \psi(\|x - \xi_j\|) + \sum_{j=1}^{NP} \alpha_{i,j+N} P_{m-1}^j(x), \quad i = 1, 2, 3 \quad (17)$$

Each variable  $u_i$  is constructed using a common set of RBF functional centres  $\xi_j$ , and the associated RBF weighting function  $\alpha_{i,j}$ . The collocation system is generated by enforcing the governing equation (13) at each internal node, and enforcing the displacement (15) and surface traction (16) operators at Dirichlet and Neumann centres respectively. The resulting collocation system may be expressed as follows (excluding the polynomial terms for brevity):

$$\begin{bmatrix}
 \psi & 0 & 0 \\
 B_{11}[\psi] & B_{12}[\psi] & B_{13}[\psi] \\
 L_{11}[\psi] & L_{12}[\psi] & L_{13}[\psi] \\
 0 & \psi & 0 \\
 B_{21}[\psi] & B_{22}[\psi] & B_{23}[\psi] \\
 L_{21}[\psi] & L_{22}[\psi] & L_{23}[\psi] \\
 0 & 0 & \psi \\
 B_{31}[\psi] & B_{32}[\psi] & B_{33}[\psi] \\
 L_{31}[\psi] & L_{32}[\psi] & L_{33}[\psi]
 \end{bmatrix}
 \begin{bmatrix}
 \alpha_1 \\
 \alpha_2 \\
 \alpha_3
 \end{bmatrix}
 =
 \begin{bmatrix}
 f_1 \\
 \tau_1 \\
 -\rho b_1 \\
 f_2 \\
 \tau_2 \\
 -\rho b_2 \\
 f_3 \\
 \tau_3 \\
 -\rho b_3
 \end{bmatrix}
 \quad (18)$$

The operators  $L_{ij}$  and  $B_{ij}$  represent the differential operators applied to  $u_i$  within the  $j^{\text{th}}$  equation of the PDE governing operator  $L$  and the surface traction operator  $B$  respectively. The functions  $L_{ij}$  and  $B_{ij}$  may therefore be expressed as:

$$L_{ij} = \mu \delta_{ij} \frac{\partial^2}{\partial x_k^2} + (\lambda + \mu) \frac{\partial^2}{\partial x_i \partial x_j} \quad i, j = 1, 2, 3 \quad (19)$$

$$B_{ij} = \lambda n_i \frac{\partial}{\partial x_j} + \mu n_j \frac{\partial}{\partial x_i} + \mu \delta_{ij} n_k \frac{\partial}{\partial x_k} \quad i, j = 1, 2, 3 \quad (20)$$

An equivalent operator for a Dirichlet boundary condition would be expressed as  $B_{ij} = \delta_{ij}$ . The collocation matrix (18) represents a square and near-fully-populated linear system. When polynomial terms are included it is of size  $n(N + NP) \times n(N + NP)$ , where  $n$  is the number of spatial dimensions,  $N$  is the number of collocation points, and  $NP$  is the number of terms in the polynomial. To extend the collocation matrix to include the polynomial terms it is necessary to include them in the substitution of equation (17) into the governing and boundary operators (13), (15) and (16).

### 3.1 RBF Finite Collocation Formulation

By generating an RBF collocation around each of the  $N_s$  stencils, formed around strictly interior nodes as indicated by Figure 1c, a series of  $N_s$  RBF collocation systems are obtained:

$$A^{(k)} \alpha^{(k)} = d^{(k)} \quad k = 1, \dots, N_s \quad (21)$$

Here  $A^{(k)}$  represents the collocation matrix for system  $k$ , and will be formed as described by equation (12) or equation (18). The data vector  $d^{(k)}$  contains the known boundary and PDE operator values, and also the unknown value of the solution field at the solution centres. Using the appropriate RBF reconstruction formula, i.e. equation (9) or equation (17), the approximate value of the field variable  $u(x)$  may be computed for any  $x$  within the support domain of system  $k$ . Expressing this computation as a vector product we have

$$u^{(k)}(x) = H^{(k)}(x) \alpha^{(k)} \quad (22)$$

where  $H^{(k)}(x)$  is identified as a reconstruction vector for system  $k$  at location  $x$ . By reconstructing the value of  $u$  at the system centrepoint,  $x_c^{(k)}$ ; i.e. the node around which system  $k$  formed (though not necessarily the geometric centre of the stencil), we obtain:

$$\begin{aligned}
u^{(k)}(x_c^{(k)}) &= H^{(k)}(x_c^{(k)}) \alpha^{(k)} \\
&= H^{(k)}(x_c^{(k)}) [A^{(k)}]^{-1} d^{(k)} \\
&= W^{(k)}(x_c^{(k)}) d^{(k)}
\end{aligned} \tag{23}$$

Here  $W^{(k)}(x_c) = H^{(k)}(x_c) [A^{(k)}]^{-1}$  is a stencil weights vector, expressing the value of the solution field  $u$  at the system centrepoint in terms of the entries in the data vector  $d^{(k)}$ . This value of  $u$  at  $x_c^{(k)}$ , as reconstructed by equation (23), appears as an unknown within the data vector of any systems which have within their stencil a solution centre located at  $x_c^{(k)}$ ; i.e. any systems which have this node on their periphery. Therefore, by performing the above reconstruction (23) for each local system  $k$ , a series of  $N_s$  simultaneous equations are formed for the  $N$  unknown values of  $u^{(k)}$  at the system centrepoints. Solution of this sparse global system therefore provides the value of  $u$  at each of the  $N_s$  internal nodes. By feeding these values back into the local data vectors,  $d^{(k)}$ , the local systems may be used to extract any other field values as may be required for post-process analysis (such as partial derivatives, or stresses in the case of linear elasticity). For more details about this highly convergent meshless collocation numerical scheme see [1].

In the sparse global assembly, the PDE governing operator and the corresponding boundary conditions of the problem have already been imposed within the local collocation systems. The number of non-zero matrix entries in each row corresponds to the number of solution centres in the associated local system; i.e. the number of nodes on the stencil periphery. Since only the peripheral nodes appear in the global system, the number of non-zero entries is smaller than for an equivalent Finite-Difference type method (see Figure 1); i.e. the sparse global matrix has a smaller bandwidth. With an appropriate sparse linear system solver the method may be scaled efficiently to very large datasets.

## 4 NUMERICAL RESULTS

Analytical results relating to rates of convergence and other numerical properties are extremely difficult to obtain for methods based on local RBF collocation. Therefore, in this work we focus on assessing the performance of the proposed finite collocation method qualitatively, using benchmark numerical problems with known analytical solutions. In each case we focus on analysing the solution accuracy and convergence rates, showing that high convergence rates may be reliably obtained.

In each numerical example we use a  $5 \times 5$  stencil configuration, with additional staggered PDE centres, as represented in Figure 1c. Larger stencil sizes may be used to obtain higher convergence rates at the expense of increased computational cost and somewhat increased sensitivity to basis function flatness (see [1]). The results presented below use a non-dimensional shape parameter of value  $c^* = 100$ , scaled against the local node separation.

### 4.1 Linear Elasticity Problem

Performance with the linear elasticity equation is assessed for a thin plate with a circular hole under uniform traction. The analytical expression for displacement and stress is given by

[16]. Here we choose material properties of  $E=210\text{GPa}$  and  $\nu=0.3$ , representing mild steel, with a hole radius  $a=1\text{m}$  and a far-field traction of  $100\text{MPa}$ . We exploit the symmetry of the problem to examine a single quadrant, constraining the solution domain to a  $4\text{m} \times 4\text{m}$  region. Over the hole we enforce the appropriate zero-traction condition, at the lines of symmetry we impose the symmetric condition, and at the far-field boundaries we enforce the analytical surface traction field, as defined by  $\tau_i = \sigma^e_{ij}n_j$ .

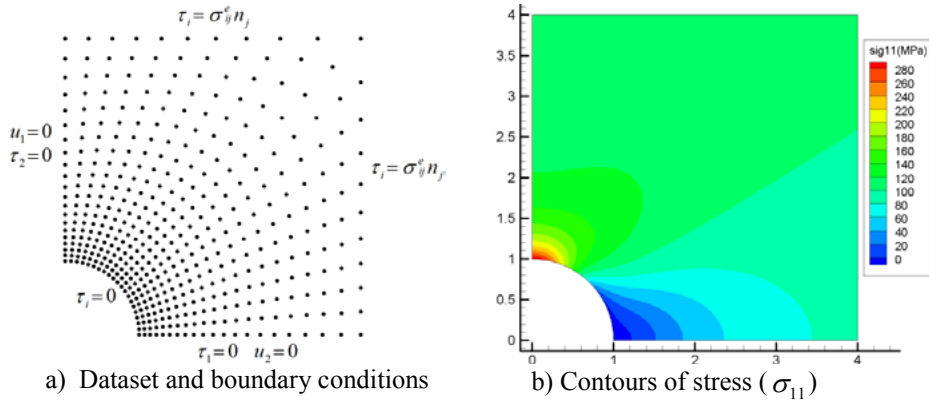


Figure 2: Dataset, boundary conditions and contours of stress, showing concentration of stresses around the hole

The dataset is generated by distributing  $N+1$  nodes over the hole, and  $N+1$  nodes in the radial direction (i.e.  $1 \leq r \leq 4$ ). A simple RBF interpolation is then performed over the domain to map this cylindrical distribution onto the full Cartesian problem domain (see Figure 2a). The resulting stresses are largely concentrated in the region around the hole, and their accurate prediction is a challenging task (see Figure 2b).

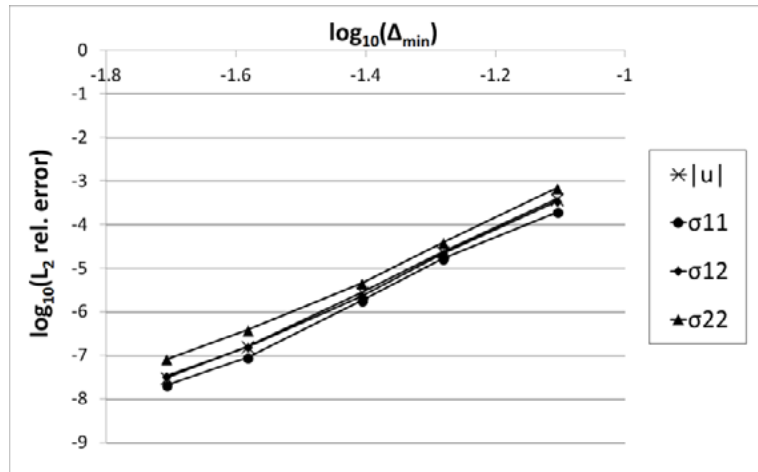


Figure 3: Spatial convergence (plate with a circular hole)

The proposed method exhibits strong spatial convergence and provides highly accurate solutions. Figure 3 shows the  $L_2$  relative error obtained from datasets of size  $N = 20, 30, 40, 60, 80$ . In this log-log plot, the gradient of the curve represents the spatial convergence rate

between successive datasets. The approximate convergence rates, obtained by line of best fit, are summarised in Table 1. The convergence rates are of orders between 6.5 and 7 for displacement and for all stress components.

$ u $	$\sigma_{11}$	$\sigma_{12}$	$\sigma_{22}$
6.90	6.79	6.75	6.56

Table 1: Approximate convergence rates (plate with a circular hole)

#### 4.1 Poroelasticity Problem

To analyse the performance of the proposed RBF-FC method with a coupled poroelasticity problem we consider a porous cylindrical annulus subject to a large internal pressure. The solution is obtained in two stages; the first stage computes the pressure field and its Cartesian derivatives at each node within the domain, by solving Darcy's equation (1). The second stage solves the inhomogeneous linear elasticity equation (7), where the inhomogeneous term is obtained from the computed pressure gradient.

For a cylindrical annulus with inner radius  $a$  and outer radius  $b$ , with pressure  $p_1$  at  $r = a$  (i.e. internal pressure) and pressure  $p_0$  at  $r = b$  (i.e. external pressure), the analytical solution for the pressure field is as given by equation (24). We set the inner pressure as  $P_1 = 100\text{MPa}$  and the outer pressure as  $P_0 = 10\text{MPa}$ .

$$p = \frac{p_0 - p_1}{\ln(b/a)} \ln(r) + \frac{p_1 \ln(b) - p_0 \ln(a)}{\ln(b/a)} \quad (24)$$

We choose a dataset of size  $(N+1) \times (N+1)$  with nodes distributed radially (see Figure 4a), and examine solution accuracy for  $N = 20, 30, 40, 60, 80$ . The Darcy flow problem is solved to a very high level of accuracy in each case, as shown in Figure 6. The analytical expression (24) is predicted to an  $L_2$  relative error of  $3.4 \times 10^{-7}$  on the  $N = 20$  dataset, and  $2.9 \times 10^{-11}$  on the  $N = 80$  dataset. Errors found in the Cartesian gradients less than a factor of two higher.

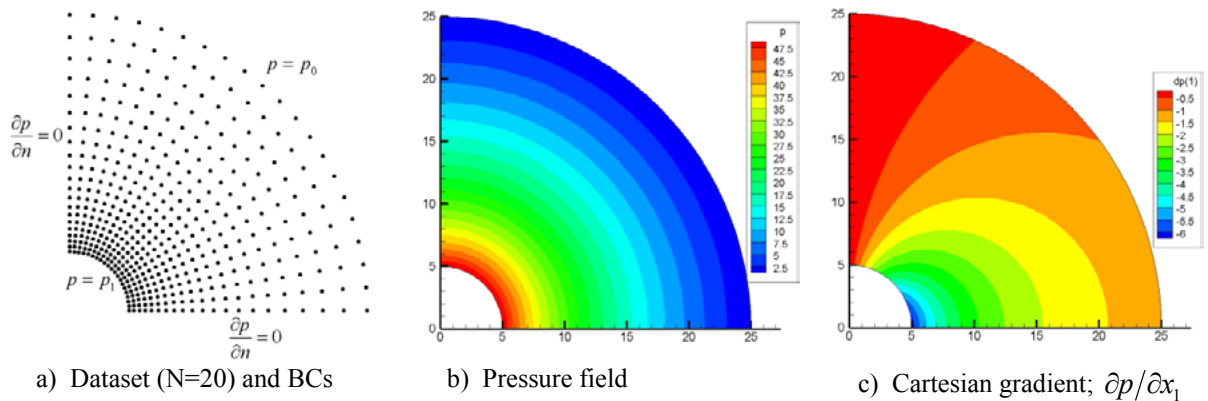


Fig 4: Darcy-flow: Dataset, boundary conditions and pressure-field representation

Following computation of the pressure-field, the inhomogenous linear elasticity equation may be solved. An analytical solution for displacement and stress may be computed as:

$$u_r = Ar + Br^{-1} + \xi_1 \left( \frac{r}{2} \ln(r) - \frac{r}{4} \right) + \xi_2 \frac{r}{2} \quad (25)$$

$$\sigma_{rr} = (\lambda + \mu) [2A + \xi_1 \ln(r) + \xi_2] - 2\mu Br^{-2} + \frac{\xi_1 \mu}{2} - \alpha p$$

$$\sigma_{\theta\theta} = (\lambda + \mu) [2A + \xi_1 \ln(r) + \xi_2] + 2\mu Br^{-2} - \frac{\xi_1 \mu}{2} - \alpha p \quad (26)$$

$$\sigma_{r\theta} = 0$$

where:

$$A = \frac{1}{2(\lambda + \mu)} \left[ \frac{p_1 a^2 - p_0 b^2}{b^2 - a^2} \left( 1 - \frac{\alpha \mu}{\lambda + 2\mu} \right) + \frac{\alpha \mu (p_1 - p_0)}{2(\lambda + 2\mu) \ln(b/a)} \right]$$

$$B = \frac{a^2 b^2 (p_1 - p_0)}{2\mu (b^2 - a^2)} \left[ 1 - \frac{\alpha \mu}{\lambda + 2\mu} \right] \quad (27)$$

$$\xi_1 = \frac{\alpha (p_0 - p_1)}{(\lambda + 2\mu) \ln(b/a)}$$

$$\xi_2 = \frac{\alpha (p_1 \ln(b) - p_0 \ln(a))}{(\lambda + 2\mu) \ln(b/a)}$$

At the  $x=0$  and  $y=0$  boundaries we enforce symmetry (i.e. zero normal displacement and zero tangential traction), and the appropriate pressure-traction condition is applied at the inner and outer surfaces (see Figure 6a). We use parameters of  $E=27.6\text{GPa}$  and  $\nu=0.15$ , representing Weber sandstone. The resulting relative errors in the displacement and stress-fields are represented in Table 2.

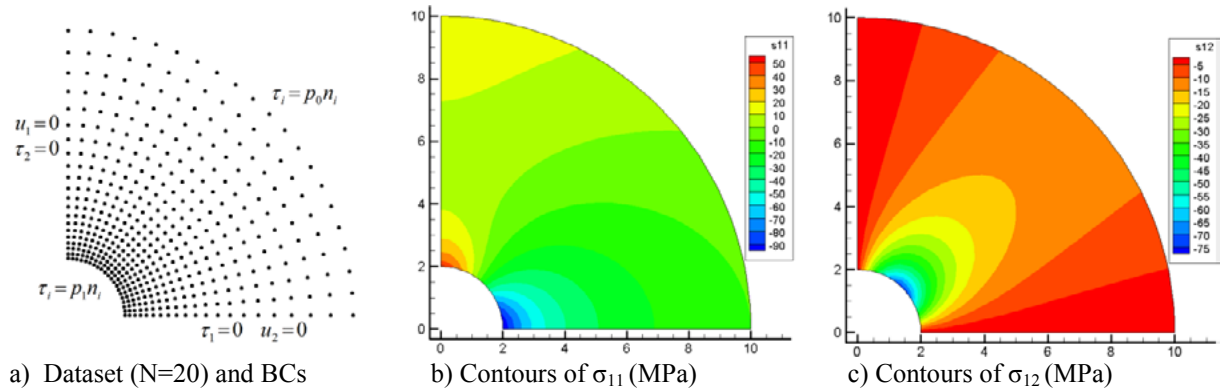
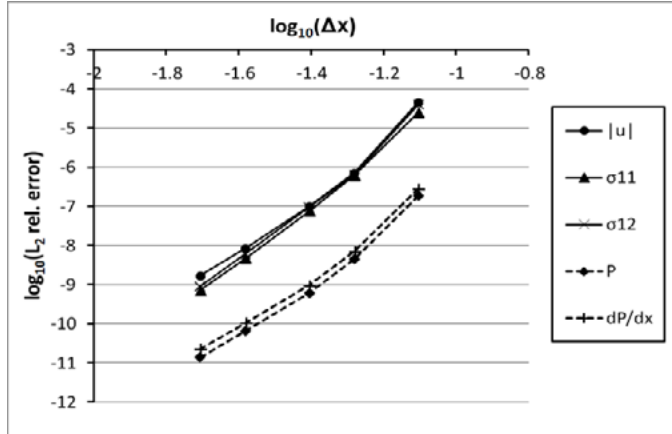


Figure 5: Boundary conditions and stress representation for poroelastic deformation

	$ u $ $L_2$ error	$ u $ max error	$\sigma_{11}$ $L_2$ error	$\sigma_{12}$ $L_2$ error	$\sigma_{22}$ $L_2$ error
$N = 20$	$4.60 \times 10^{-5}$	$1.45 \times 10^{-4}$	$2.48 \times 10^{-5}$	$4.01 \times 10^{-5}$	$2.48 \times 10^{-5}$
$N = 30$	$7.19 \times 10^{-7}$	$1.66 \times 10^{-6}$	$6.12 \times 10^{-7}$	$6.49 \times 10^{-7}$	$6.12 \times 10^{-7}$
$N = 40$	$9.97 \times 10^{-8}$	$2.52 \times 10^{-7}$	$7.53 \times 10^{-8}$	$9.50 \times 10^{-8}$	$7.53 \times 10^{-8}$
$N = 60$	$8.34 \times 10^{-9}$	$2.00 \times 10^{-8}$	$4.65 \times 10^{-9}$	$6.08 \times 10^{-9}$	$4.65 \times 10^{-9}$
$N = 80$	$1.65 \times 10^{-9}$	$3.41 \times 10^{-9}$	$7.01 \times 10^{-10}$	$8.90 \times 10^{-10}$	$7.01 \times 10^{-10}$

Table 2: Relative errors for stress and displacement at varying dataset density

Figure 6: Spatial convergence;  $L_2$  relative errors against minimum node separation

Errors are low for each examined dataset, with strong reductions in error observed as the dataset is refined. On the finest  $N = 80$  dataset we observe errors of order  $10^{-9}$  to  $10^{-10}$ . Errors for the stress field are, in each case, of similar magnitude to errors observed in the displacement field. The maximum relative displacement error is never more than a factor of four larger than the average relative error taken using the  $L_2$  norm. The spatial convergence is represented in Figure 6; taking a line of best fit average we see that the convergence rate is roughly seventh order for each of the examined fields (displacement, stress, and pressure).

## 5 CONCLUSIONS

A high-resolution meshless numerical solution has been described for coupled poroelastic analysis, based on the RBF finite collocation (RBF-FC) approach. The poroelastic analysis procedure begins with the solution of Darcy's equation, in order to obtain the fluid-pressure field throughout the domain. From this solution the pressure gradient is computed at each internal node, and is used as an inhomogeneous term for the linear elasticity equation. By solving this equation with appropriate pressure-traction boundary conditions, the displacement and stress fields may be obtained for the full poroelastic problem.

The RBF-FC method allows highly accurate solutions to be obtained. The RBF-FC solution procedure has been demonstrated for a benchmark linear elasticity test case, for the solution of Darcy's equation, and for a coupled poroelastic problem. In each of the cases examined the method is able to produce highly accurate solutions, even on relatively coarse datasets, and demonstrates better than sixth order convergence in each case.

## ACKNOWLEDGEMENTS

This work was funded by the MUSTANG EU project (contract number 227286), which investigates the long-term geological storage of CO<sub>2</sub>

## REFERENCES

- [1] Stevens, D.; Power, H.; Meng, C, Y.; Howard, D. & Cliffe, K. , An alternative local collocation strategy for high-convergence meshless PDE solutions, using radial basis functions *J. Comput. Phy*, 2013, (*submitted*)
- [2] E. J. Kansa. Multiquadrics - a scattered data approximation scheme with applications to computational fluid-dynamics-i: Surface approximations and partial derivatives estimates. *Comput. Math. Appl.*, 19:127–145, 1990.
- [3] E. J. Kansa. Multiquadrics - a scattered data approximation scheme with applications to computational fluid dynamics-ii: Solution to parabolic, hyperbolic and elliptic partial differential equations. *Comput. Math. Appl.*, 19:147–161, 1990.
- [4] B. Sarler and R. Vertnik. Meshless explicit local radial basis function collocation methods for diffusion problems. *Comput. Math. Appl.*, 51:1269–1282, 2006.
- [5] G. Wright and B. Fornberg. Scattered node compact finite difference-type formulas generated from radial basis functions. *J. of Comput. Phys.*, 212:99–123, 2006.
- [6] E. Divo and A. Kassab. An efficient localised radial basis function meshless method for fluid flow and conjugate heat transfer. *Journal of Heat Transfer*, 129:124–136, 2007.
- [7] D. Stevens, H. Power, M. Lees, and H. Morvan. The use of PDE centres in the local RBF Hermitian method for 3D convective-diffusion problems. *J. Comput. Phys.*, 228:4606–4624, 2009.
- [8] Biot M.A., (1941), General theory of three dimensional consolidation, *Journal of Applied Physics*, Vol. 12 (2), 155-164
- [9] A.S.M. Wong, Y.C. Hon, T.S. Li, S.L. Chung, and E.J. Kansa. Multizone decomposition for simulation of time-dependent problems using the multiquadric scheme. *Comput. Math. Appl.*, 37:23–43, 1999.
- [10] Z. Wu. Hermite-Birkhoff interpolation of scattered data by radial basis functions. *Approximation Theory and its Applications*, 8:1–11, 1992.
- [11] E.J. Kansa and R.E. Carlson. Improved accuracy of multiquadric interpolation using variable shape parameters. *Comput. Math. Appl.*, 24:99–120, 1992.
- [12] J. Wertz and E.J. Kansa. The role of the multiquadric shape parameters in solving partial differential equations. *Comput. Math. Appl.*, 51:1335–1348, 2006.
- [13] M. Zerroukat, H. Power, and C.S. Chen. A numerical method for heat transfer problems using collocation and radial basis functions. *International Journal for Numerical Methods in Engineering*, 42:1263–1278, 1998.
- [14] Y.C. Hon and X.Z. Mao. A radial basis function method for solving options pricing modelling. *Financial Engineering*, 8:31–50, 1999.
- [15] Y.C. Hon, K.F. Cheung, X.Z. Mao, and E.J. Kansa. A multiquadric solution for shallow water equation. *ASCE J. Hydraulic Engineering*, 125:524–533, 1999.
- [16] S. Timoshenko and J. Goodier. *Theory of Elasticity*. McGraw-Hill, New York, 1951.